Reducing the wave induced loading of tidal turbine blades through the use of a flexible blade

Reducing the wave induced loading of tidal turbine blades through the use of a flexible blade

Susan Tully[1], Ignazio Maria Viola[1]*

ISROMAC 2016

International Symposium on Transport Phenomena and Dynamics of Rotating Machinery

Hawaii, Honolulu

April 10-15, 2016

Abstract

A study into the loading effects of wave-current interactions on a blade section of a horizontal axis tidal turbine was performed. Wave-current interactions were calculated based on 2nd order linear wave theory and a numerical model for estimating loads on both rigid and flexible blade sections is presented, based on a quasi-steady analysis. Results from this model are compared with load measurements on two constant cross-section hydrofoils, one rigid and one flexible, in combined waves and currents in order to assess whether a flexible blade can lead to lower load fluctuations. Particle image velocimetry was used to investigate the flow field surrounding the hydrofoils throughout a wave period in order to better understand the underlying hydrodynamics. The flow experienced by each hydrofoil is found to be highly unsteady with hysteresis effects resulting in different loading profiles than the quasi-steady analysis predicts. The experimental results indicate that the oscillating pressure field, associated with an oscillating free surface, significantly changes the hydrodynamic behaviour of the hydrofoils. The flexible blade was found to reduce the magnitude of load fluctuations in addition to achieving higher lift to drag ratio as compared to its rigid counterpart.

Keywords

Tidal turbine hydrodynamics — Unsteady flow — airfoil in oscillatory flow — Wave-current interaction — flexible blade

[1] *Institute for Energy Systems, School of Engineering, University of Edinburgh, United Kingdom*

***Corresponding author**: i.m.viola@ed.ac.uk

INTRODUCTION

Tidal turbines must operate within an unsteady flow environment. The combination of diurnal currents, sheared current profiles, high levels of turbulence and wave-current interaction leads to highly variable flow across devices (see figure 1), with an associated variation in the loads experienced. Whilst this has ramifications both on the ability of a turbine to generate power efficiently and on the expected lifespan of a device, a lack of understanding of unsteady turbine hydrodynamics has lead to some developers choosing to over-engineer their devices by as much as 30% [1]. Of particular note is the effect of cyclical wave-induced loading on devices since their cyclical nature means that blade and rotor fatigue becomes an increasingly important issue. For example, the large fetch provided by the North Atlantic means that UK wave climates are highly energetic, leading to wave-induced velocity oscillations strong enough to propagate through the water column to typical turbine deployment depths. The European Marine Energy Centre (EMEC) reported that wave-induced velocities could be felt as deep as 20 m below the free surface [2]. Further more, as a turbine blade rotates, and passes through the depth-dependent wave-induced flow field, the blade will experience an additional cyclical loading effect with a period of the blade rotation. These wave-induced loadings can decrease the life of a turbine blade to 30 months, when the expected lifetime is of the order of 30 years.

Recent reviews [3] and [4] indicate that flexible foils have shown promise within the wind energy industry in reducing the increasingly large load fluctuations associated with the ever increasing turbine diameters. Given the high fluid density of water, and the likelihood of tidal turbines experiencing cyclical flow, flexible blades require further investigation in order to decide on their capacity to reduce loads within a tidal environment and thus increase the life time of next generation tidal turbines.

The loading of horizontal axis tidal turbines has been an active research question for a number of years though the vast majority of work has gone into quantifying and understanding steady-state loading. Of the few studies which have looked into unsteady loading behaviour, investigations have focused on torque and thrust measurements of turbines as a whole. Two such investigations by Barltrop *et al.* [5] and Galloway *et al.* [6] both found significant variations in instantaneous thrust and torque magnitudes through a wave period, greater than 35% of the mean rotor load; though smaller difference to average power coefficients as compared to a current only case. Luznik *et al.* [7], in corroborating these findings, also noted that the presence of waves raised the lower threshold of the operable tip speed ratio (*TSR*) range due to the variations in torque produced. Since these studies were investigating rotor-scale loading it is difficult to draw any conclusions on the flow and loading experienced by individual blades.

Milne *et al.* [8] recognised that individual blades were likely to undergo more severe loading cycles than the rotor as a whole, where the torque and thrust behaviour was in effect an averaging of the forces incident on the three blades. They investigated blade scale loads via instrumented blades on a scaled turbine rotating in planar oscillating flow. While

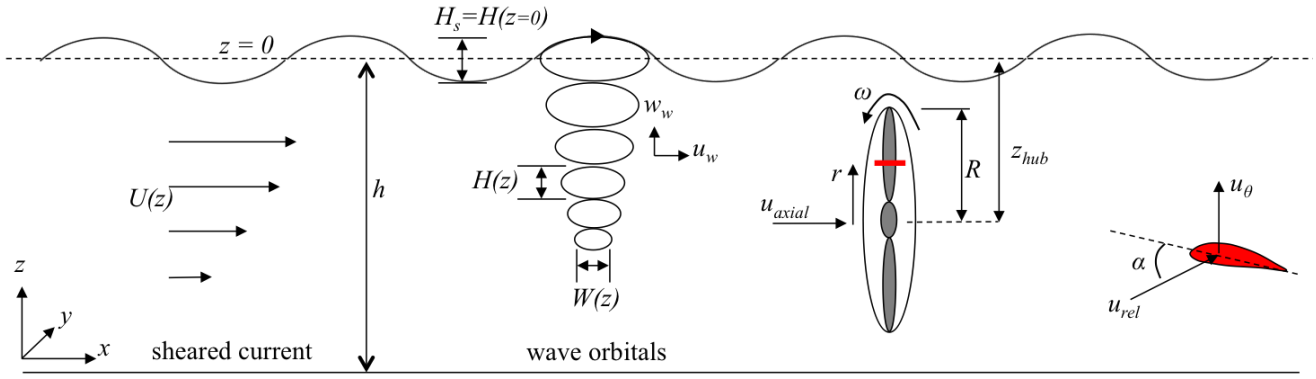

Figure 1. Onset flow experienced by a tidal turbine blade section

they found increased loads associated with separated flow, and evidence of approximately 25% greater loads during dynamic stall for certain wave conditions, their use of an unsteady flow which was uniform over the rotor plane meant that their investigation lacked any conclusion on the effects of each blade's rotating through a depth-dependant wave field.

In 2014 Galloway *et al.* [9] instrumented one of the blades of their scaled turbine in order to investigate blade-scale dynamic loading induced by waves and also investigated a depth-dependent wave field. They found that wave frequency, not height, was the driving force behind wave-induced loadings. In addition, they found that dynamic stall had little effect for the wave conditions they tested, both experimentally and numerically where they used the Boeing-Vertol model developed by Tarzanin [10]. This result is in disagreement with the results of Milne, despite both testing a similar scale device, at similar frequencies and oscillation amplitudes. What differed between the two analyses is that while Milne tested under purely planar oscillatory flow by towing their turbine at a sinusoidally oscillating velocity in stall water, Galloway towed their device through a wave field. This means that Galloway's tests included the effects of both a dynamically varying flow field and additionally the oscillations of static pressure from the free surface displacement. Whether this differing dynamic pressure field was the cause for the difference in loadings is still an open research question.

These investigations into the unsteady loading of tidal turbines focused on investigating the effects of the largest and longest waves and relied on load measurements alone, with no corresponding flow visualisation techniques used to further elucidate the hydrodynamic cause of the loading. Of course, oscillatory flow over airfoils has been studied extensively, especially for propulsion with most papers taking a Particle Image Velocimetry (PIV) based approach. The majority of studies have either actively pitched or plunged a foil in a steady current or towed it in waves only, as is also the case in each paper listed above. Neither approach is a true representation of the flow field as would be experienced by a tidal turbine blade in real ocean conditions, where higher order wave-current interaction effects alter the mean vertical velocity profile [11] and the oscillation in free surface height is out of phase with the change in dynamic pressure.

In this paper the hydrodynamics of the wave-blade interaction is studied, for both a rigid and flexible blade section, using a combined wave and current tank which naturally incorporates the higher order effects expected for real ocean conditions. The aims of this paper are two fold. First is to investigate whether a flexible tidal turbine blade could achieve a more favourable loading profile, as compared to the more standard rigid blade. Second, to answer the question of whether or not the oscillation in static pressure caused by ocean waves has any effect on the hydrodynamic behaviour of submerged hydrofoils.

To address these aims, this paper investigates the unsteady flow perturbations experienced by individual tidal turbine blade sections when exposed to wave-induced oscillatory flow, utilising both numerically and experimentally derived loadings alongside PIV flow visualisation. In addition a novel flexible blade design is presented which has been designed to reduce the amplitude of load fluctuations experienced through passively flexing the trailing edge section.

1. METHOD

1.1 Construction of the flow experienced by a blade section

The flow scenario is presented in figure 1, including the coordinate systems used. Whilst the problem is highly three dimensional, insights can be obtained considering the flow incident on a blade section from a rotating reference frame moving with the blade. The parameters of interest are then the relative velocity incident on the hydrofoil U_{rel}, the angle of attack α between the blade chord c and U_{rel}, and the reduced frequency k_f of the flow oscillation. U_{rel} varies with time t and it is a function of the current U_0, the wave orbital velocity components u_w and w_w in the x and z directions, respectively, the angular velocity of the blade ω and the radial distance r of the blade section from the turbine axis. The reduced frequency

k_f has been defined as $k_f = 2\pi f c/U_0$, where f is the wave frequency. Thus, for $k_f = \pi/2$ and π, a particle of fluid moving at U_0 would convect $x/c \approx 4$ and $x/c \approx 2$ in one wave period, respectively. Wave velocities, u_w and w_w are calculated using 2nd order linear wave theory [12], equations (1) and (2), ensuring that the wavenumber $k = 2\pi/\lambda$ is calculated from the doppler shifted dispersion relation $\sigma = U_0 k + \sqrt{gk\tanh(kh)}$; where λ is the wavelength, $\sigma = 2\pi f$ as measured by a static wave buoy, g is the gravity acceleration and h the water depth. If dealing with waves propagating counter to the current direction then u_w changes sign, therefore the ± in equation (1) stands for opposing and following waves respectively. Only waves which satisfy the Stokes limit of maximum steepness of $H_s/\lambda = 1/7$ should be included, while any with $k \leq 0$ should be assumed blocked. Here, H_s refers to the peak-to-trough wave height.

$$u_w = \frac{H_s}{2}\frac{gk}{\sigma}\frac{\cosh k(h+z(t))}{\cosh kh}\cos(kx \pm \sigma t) + \frac{3}{16}\frac{H_s^2\sigma k\cosh 2k(h+z(t))}{\sinh^4(kh)}\cos 2(kx \pm \sigma t) \quad (1)$$

$$w_w = \frac{H_s}{2}\frac{gk}{\sigma}\frac{\sinh k(h+z(t))}{\cosh kh}\sin(kx \pm \sigma t) + \frac{3}{16}\frac{H_s^2\sigma k\sinh 2k(h+z(t))}{\sinh^4(kh)}\sin 2(kx \pm \sigma t) \quad (2)$$

When investigating the flow experienced by a blade cross section as it rotates, x remains constant while $z(t)$ is time dependant to account for the blade rotation through the depth dependant wave field $z(t) = z_{\text{hub}} + r\sin\omega t$. The decay of wave orbital dimensions $H(z)$ and $W(Z)$ below the free surface are given in equations (3) and (4) respectively.

$$H(z) = \frac{H_s}{2}\frac{\sinh k(h+z)}{\sinh kh} \quad (3)$$

$$W(z) = \frac{H_s}{2}\frac{\cosh k(h+z)}{\sinh kh} \quad (4)$$

For stationary, cylindrical coordinates the parameters of interest on the rigid blade section at distance r out from the hub are defined in equations (5 - 8).

$$u_{\text{axial}} = U_0 + u_w \quad (5)$$

$$u_\theta = \omega r + w_w\cos\omega t \quad (6)$$

$$U_{\text{rel}} = \sqrt{{u_{\text{axial}}}^2 + {u_\theta}^2} \quad (7)$$

$$\alpha = 90^\circ - \arctan\frac{u_\theta}{u_{\text{axial}}} - \beta \quad (8)$$

where β is the static blade pitch, which is the angle between the rotor plane and the blade chord.

The antisymmetric NACA 4415 airfoil profile was chosen for this study given its use in the PerAWAT project [13] for scale model tests designed to replicate the behaviour of Alstom Power's (then Tidal Generation Ltd) turbine. Extensive data on the performance of the NACA 4415, under steady flow conditions and at similar Reynolds number ($Re = 8\times10^4$), can be found in [14].

1.2 Quasi-static numerical model

The loads on the rigid hydrofoil are calculated based on the steady-state normal force coefficient, as defined in equation (9), for the NACA 4415 profile used in this study, taken from [14].

$$C_n = \frac{F_n}{\frac{1}{2}\rho U_{\text{rel}}^2 cb} \quad (9)$$

where F_n is the normal force, ρ the density of the fluid, c the chord length and b the span. Under fully steady conditions, with $U_{\text{rel}} = U_0$, the normal force coefficient C_n increases linearly within the attached flow region, from $C_n = -0.7$ at $\alpha = -10^\circ$ to $C_n = 1.4$ at $\alpha = 10^\circ$. For $\alpha < -10^\circ$ and $\alpha > 10^\circ$, C_n is set to remain constant, at the minimum and maximum value respectively, to replicate the early stall behaviour. The loads on the rigid hydrofoil are then scaled according to α as calculated in equation (8). The load on the flexible blade is computed taking account of the passive deflection of the trailing edge which changes the direction of the chord, which is defined as the line through the leading and trailing edge of the blade section; therefore a displacement of the trailing edge leads to a variation of β and thus of α. The flexible section of the foil is represented as a cantilever beam, fixed at one end, with a uniformly varying load to mimic the pressure difference between the pressure and suction sides of the hydrofoil along the flexible length of the chord. A schematic is given in figure 2.

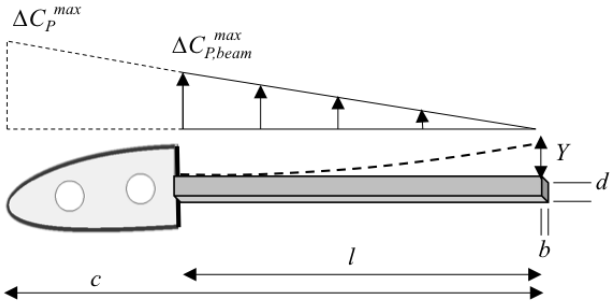

Figure 2. Cantilever beam representation of the flexible blade

The maximum difference between the pressure coefficient on the suction and pressure sides of the hydrofoil $\Delta C_{\text{P,beam}}^{\text{max}}$, occurs at the fixed end of the cantilever beam and is related to the maximum coefficient of pressure difference at the leading edge of the hydrofoil $\Delta C_{\text{P}}^{\text{max}}$ by equation (10), where $l = \frac{2}{3}c$ is the length of the flexible part of the foil.

$$\Delta C_{\text{P,beam}}^{\text{max}} = \frac{l}{c}\Delta C_{\text{P}}^{\text{max}} \quad (10)$$

The pressure difference decays linearly along l to zero at the trailing edge. This triangular ΔC_P distribution can be seen in [14] for the NACA 4415 over a broad range of attached flow conditions with $\Delta C_{\text{P}}^{\text{max}} = 3$ at $\alpha = 10^\circ$. The magnitude of the trailing edge deflection Y can then be computed as in equation (11); with inertia $I = d^3/12$, beam thickness d and Young's

Modulus E. The Young's Modulus of the rigid and flexible blades are 3000 MPa and 0.97 MPa respectively.

$$Y = \frac{3}{2}\frac{\rho u_{\text{rel}}^2 b l^5}{30EIc} \tag{11}$$

This trailing edge deflection is then used to calculate α for the flexible blade. Since this change in α would lead to a change in hydrodynamic load, an iterative fluid-structure coupling is implemented in order to calculate the load at every time-step. Treating each time step individually and keeping the flow conditions constant, the numerical model loops through calculating the hydrodynamic load, and corresponding deflection, until both are in equilibrium for that time step.

1.3 Experimental test

A rigid and a flexible hydrofoil were manufactured on an Objet500 Connex multi-material 3D printer (16 μm layer accuracy) using PolyJet^{TM} VeroWhitePlus RGD835 and TangoBlackPlus FLX980 materials. TangoBlackPlus is a flexible, rubber-like material which can be mixed in different ratios with VeroWhitePlus to produce differing grades of flexibility.

The flexible blade is developed around a flexible rubber hinge with $l = \frac{2}{3}c$ as in the numerical section, allowing the trailing edge to flex in response to pressure changes in the surrounding flow. The first third of the hydrofoil is rigid while the latter two thirds are free to flex by incorporating a thin split on the pressure side such that the trailing edge section can slide back and fourth along the underside of the rigid leading edge section, without major changes to the profile. A schematic of the flexible blade is shown in figure 3. Both hydrofoils have $c = 0.15$ m and $b = 0.3$ m.

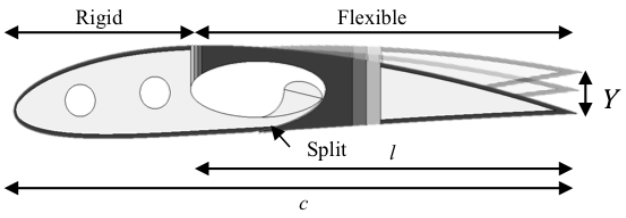

Figure 3. Schematic diagram of the cross-section of the flexible blade

A schematic of the setup within the University of Edinburgh's combined wave and current flume is given in figure 4. The flume is 8 m long, 0.4 m wide and up to 0.45 m deep and is capable of generating following and opposing waves with current [15]. For this study, only opposing waves are tested experimentally in order to be able to include a series of turbulence reducing meshes near the inlet, reducing the turbulence intensity to approximately 3% at $U_0 = 0.5$ m/s. Waves are tested at a frequency $f = 1$ Hz, and wave height $H_s = 0.09$ m leading to a peak-to-trough α oscillation of 24°. The test-section is 5 m downstream of the inlet (4 m downstream of the last mesh screen). The hydrofoil is mounted horizontally at mid-depth, such that the quarter chord position is at $z_{foil} = 0.225$ m below the free surface and is sandwiched between two vertical clear acrylic splitter plates, placed to negate tip loss effects. The foil is attached to the splitter plates via an 8 mm stainless steel rod which threads through both splitter plates and the full span of the foil. There is a 1 mm gap between the hydrofoil and each splitter plate, achieved via placing a washer on the rod between the splitter plate and foil which allows the flexible blade to deflect. There is also a 95 mm gap between the plates and the flume side-walls in order to remain clear of the boundary layer on these walls. Hydrofoils are mounted at $\beta = 10°$ static pitch.

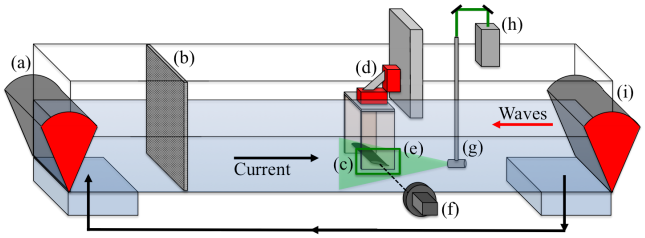

Figure 4. Schematic of experimental setup: (a) wave absorbing paddle; (b) turbulence reducing meshes x4; (c) hydrofoil; (d) load cells; (e) PIV laser light sheet and image capture window; (f) PIV camera; (g) laser beam expander; (h) laser; (i) wave making paddle.

Force measurements are taken with two Honeywell Low Range Precision Miniature resistive Load Cells (model 31, 45N for drag and model 34, 1110N for lift) mounted in KineOptics WTB 3.0 parallelogram mounts above the splitter plates, connecting them to the rigid rig frame such that they measure the forces on the hydrofoil and splitter plates combined. The load cells are mounted perpendicular to one and other in order to measure both the vertical and horizontal forces simultaneously. The signals from the load cells were amplified by two DC powered Mantracourt SGA/D amplifiers fed into a 16-bit National Instruments board. Signals were post-processed in Matlab 8.5.0 after having first been low-pass filtered at 30 Hz in LabView to remove unwanted noise.

The PIV system used consists of a pulsed dual-cavity Nd:YAG laser with 200 mJ at 532 nm and a maximum pulse rate of 15 Hz; with a CCD IMPREX 50MP camera with 2448 x 2050 pixel resolution, mounted outside the flume with the image plane parallel to the free stream flow. The camera has a max frame rate of 50 frames/s but the buffer download speed limits this to 15 frames/s, leading to a maximum PIV image frequency of 7.5 Hz. A Nikkor $f/2.8$, 50 mm lens is used to achieve a sufficiently shallow depth of field, with a 532 nm monochromatic filter installed in order to minimise the noise from ambient light. As a further noise reduction measure the rigid hydrofoil is painted matt black in order to minimise reflections, while the flexible blade's matt black rubber coating means no painting is required. The laser is mounted vertically above the flume, requiring direction over three mirrors and through a beam expander in order to align the laser sheet parallel with the flow direction. The laser sheet

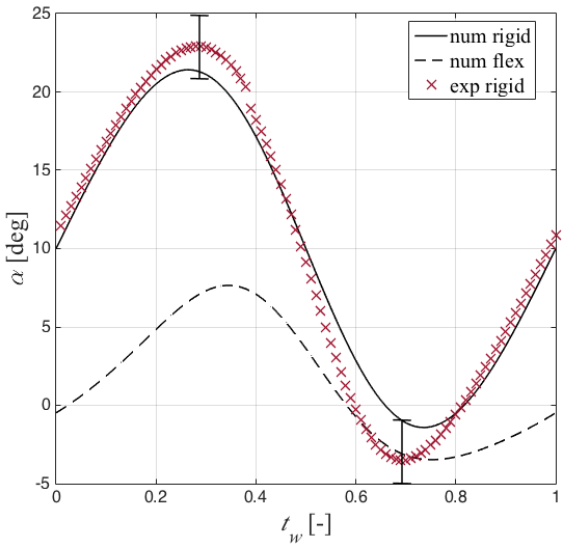

Figure 5. Angle of attack experienced by the hydrofoil during a wave period as measured in front of the hydrofoil (exp rigid); and predicted numerically for a rigid (num rigid) and a flexible foil (num flex).

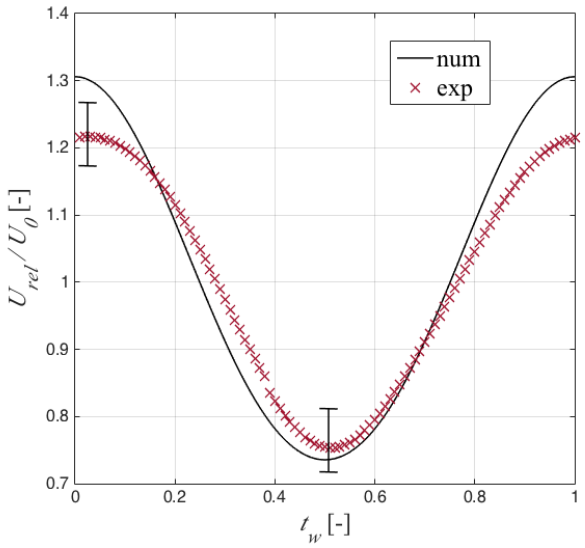

Figure 6. Measured (exp) and predicted (num) flow speed experienced by the hydrofoil during a wave period.

is approximately 4 mm thick, centred at the quarter chord depth, with the sheet axis aligned at -5° below the horizontal in order to minimise free surface reflections from the waves. The light sheet is positioned at one third span from the camera facing side of the hydrofoil. Conduct-O-Fil silvered spheres are used to seed the flow with an average diameter of 14 μm and average density of 1.7(g/cc).

Load cell and PIV data are recorded for 20s intervals, capturing 20 wave periods for the 1 Hz wave frequency used. The current is initialised 20 s prior to wave generation and then 6 wave peaks are allowed to pass the hydrofoil before recording begins and the flume is allowed to settle before the next measurement is taken. As the loads measured include a contribution from the splitter plates, loads were measured for the splitter plates alone and the mean, over one wave period, subtracted from the results. The loads are measured at a sampling frequency of 150 Hz in order to allow for direct comparison with the PIV images (7.5 Hz frequency). The average intensity is subtracted from each PIV image set prior post-processing. Vector fields are then calculated using 3-pass adaptive correlation with square, 32 pixel, interrogation windows at 50% overlap and any ensemble averages are generated from a minimum of 9 wave periods worth of data.

The conditions tested experimentally are listed in table 1, where ν stands for the kinematic viscosity of the water and the other symbols have been introduced above. H_s in table 1 is that set in the numerical model to achieve an α oscillation comparable with the experimental results while U_0 is the mean flow velocity in the x direction measured at z_{foil} for combined waves and currents.

Table 1. Test conditions

Paremeter	Value
Reynolds number $(Re = \frac{U_0 c}{\nu})$	75,000
Froude number $(Fr = \frac{U_0}{\sqrt{g H_s}})$	0.53
Reduced frequency $(k_f = \frac{2\pi f c}{U_0})$	1.9
Steepness $(\frac{H_s}{\lambda})$	0.04
Depth/chord ratio $(\frac{-z_{foil}}{c})$	1.5
Relative depth (kh)	1.27
Elastic parameter, rigid $(\gamma_F = \frac{E_F d_F^3/12}{0.5\rho U_0^2 l_F^3})$	0.13
Elastic parameter, flexible $(\gamma_R = \frac{E_R d_R^3/12}{0.5\rho U_0^2 l_R^3})$	2.3×10^4

2. RESULTS AND DISCUSSION

2.1 Loads on a blade section

Figures 5 - 7 show the results from the numerical model and experimental test conditions for both the rigid and flexible blades. The markers denote the phase averaged experimental results whilst the predictions from the numerical model are denoted by lines. The results are plotted versus time (t) normalised with the wave period, $t_w = tf$. In addition, the error bars on figures 5 and 6 give the spread of α and U_{rel} respectively at a confidence level of 95%. The turbulence in the flume, combined with the large waves required to generate suitable α oscillations, led to some discrepancy in flow conditions one wave period to the next. This is reflected in the size of the error bars drawn.

The computed α oscillation shown in figure 5 for the rigid hydrofoil has been matched to the magnitude of the α oscillation measured in the experiments while the flexible hydrofoil experiences an entirely different α oscillation as the

deflection of the trailing edge changes α. Both hydrofoils were mounted at a static pitch of 10° and the rigid hydrofoil oscillates around this value. However the flexible hydrofoil oscillates around a smaller mean α as the trailing edge initially deflects upwards in response to the force from the current. The rigid blade undergoes a peak-to-peak α oscillation of 25° while the flexible blade only experiences half of this, with a peak-to-trough α oscillation of 12°.

The comparison between measured U_{rel} and that predicted be the numerical model is given in figure 6. The numerical model over predicts the amplitude of the velocity oscillation. Bearing in mind that the numerical wave height was set to match the α oscillation measured, this over-prediction is likely due to the wave velocities being calculated based on linear wave theory where waves are purely sinusoidal. In reality higher H_s waves are steeper in the crests and shallower in the troughs. Remembering that the experimental case involved the current and wave field travelling in opposite directions such that the maximum U_{rel} corresponds to a wave trough and the minimum to a wave peak, thus the free surface elevation is minimum at $T_w = 0$ and maximum at $T_w = 0.5$, while U_{rel} is maximum at $T_w = 0$ and minimum at $T_w = 0.5$.

The variation in C_n, as defined in equation (9), is given in figure 7. The numerical code, based on a quasi-steady analysis predicts that the rigid blade will be in stall for the first half of the wave period, while the experimental results show that C_n continues to rise, despite α reaching upwards of 15°, well past the steady state stall angle. This agrees with the current understanding of unsteady loading and dynamic stall in that the normal operational window on α is extended and that separation occurs at higher angles of attack than would be expected from steady state results. In addition for the last quarter of the wave period, the numerical model vastly over predicts the loading on the blade; this is due to flow separation on the upper side of the hydrofoil as will be shown in the following section 2.2.

The variation of the normal force coefficient with the angle of attack is shown in figure 8. The computed trends for the rigid and flexible blades are the same but extend for different intervals of α, roughly $-1° < \alpha_R < 22°$ and $-3° < \alpha_F < 7°$. C_n increases linearly up to a plateau for $\alpha > 10°$. The flexible blade agrees quite well with the numerical prediction, as also shown in figure 7, and does not present any hysteresis loop. On the contrary, the rigid blade shows a clear hysteresis loop which is traveled anti-clockwise. At $T_w = 0$, under the wave trough, $\alpha \approx 10°$ and $C_n \approx 0.5$; with the increase of the free surface elevation both α and C_n increase and C_n overshoots the maximum predicted for quasi-steady conditions. In this initial part of the wave period, C_n is much lower than predicted because of the large trailing edge vortex that will be discussed in the next section. After having reached the maximum C_n, α begins to decrease and C_n decreases as well, but at a lower rate than it increased because trailing edge separation is no longer present on the upper side of the hydrofoil.

While the mean C_n for the rigid hydrofoil is higher than that of the flexible hydrofoil, the magnitude of the load fluctuations

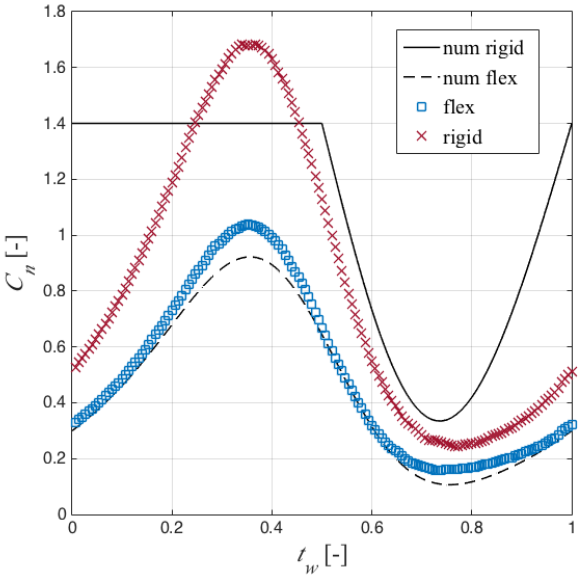

Figure 7. Normal force coefficient during a wave period.

is also higher. In this respect the flexible hydrofoil has achieved its performance aim, that of reducing the load fluctuations on a tidal turbine blade. The fact that the mean C_n for the flexible blade is lower than that of the rigid blade does not imply that there would be a performance loss if a tidal turbine were to use a flexible blade. In fact each blade section should operate at the maximum lift/drag ratio condition in order to maximise the energy extracted, and thus a higher C_n is not necessarily desirable. The time average over a wave period of the lift over drag ratio for the rigid blade is $L/D_R = 8$ while for the flexible blade it is $L/D_F = 10.7$. Therefore, while the mean C_n is lower for the flexible blade, its lift over drag ratio is higher and so could lead to a higher power output under the right design and operating conditions. Another point to add is that losses due to drag are what limit the maximum possible design TSR [16]. The flexible blade will allow for a higher ceiling on the maximum possible TSR, since its drag losses are lower, allowing for more power output.

2.2 Flow fields around a blade section

The time averaged velocity fields around both the rigid and flexible hydrofoils are given in figure 9. The greyed out region on the bottom image covers the region over which the trailing edge deflected throughout the recording. The large degree of trailing edge separation experienced by the rigid hydrofoil can be seen in the velocity deficit behind the hydrofoil which is not present for the flexible blade. This is because the rigid hydrofoil experiences a much larger α oscillation and goes some way towards explaining the lower load fluctuations experienced by the flexible hydrofoil.

To investigate further, figure 10 gives the velocity field around each foil at key points within a single, ensemble averaged, wave period t_w. Images are ensemble averages of all flow fields captured in 5° bins at key points through the

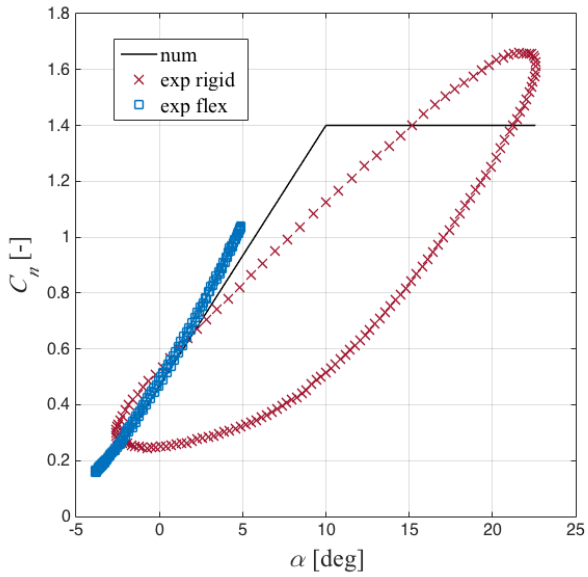

Figure 8. Normal force coefficient versus angle of attack.

wave period as indicated in the insert. The angle of attack and velocity is that measured at the leading edge position of the foil. What is not shown in the PIV images is what is happening to the pressure field, along the chord of the hydrofoil, caused by the free surface displacement. The static pressure varies according to the free surface displacement such that the maximum corresponds to a wave crest and the minimum to a wave trough. Therefore the maximum wave-induced pressure gradient ($\partial p_w/\partial x$) is at $t_w = 0.25$ and minimum at $t_w = 0.75$. From the momentum equation it can be observed that $\partial p_w/\partial x = -\rho Du_x/Dt$. Therefore, from the derivative of U_{rel}/U_0 in figure 6, it can be estimated that $\partial p_w/\partial x \approx 750$ Pam^{-1}, which is about one q/c, where $q = 1/2\rho U_0{}^2$ is the reference dynamic pressure of the tidal stream. Recalling the triangular distribution of ΔC_P along the foil chord, it can be estimated that the quasi-static pressure gradient on the upper side of the foil $\partial p_0/\partial x$ is about $5q/c$ when α is maximum at $t_w = 0.25$ and negligible when α is minimum at $t_w = 0.75$. Therefore the boundary layer on the upper side of the foil experiences a maximum (adverse) pressure gradient, which promotes separation, of about $6q/c$ at $t_w = 0.25$ and a minimum (favourable) pressure gradient of about $-q/c$ at $t_w = 0.75$. The numerical model accounts only for $\partial p_0/\partial x$ and neglects $\partial p_w/\partial x$.

The adverse pressure gradient is at its maximum between images B and C and is the cause of the small separation bubble that can be seen in figure C for the rigid blade, roughly half way along the chord. As time progresses, this separation convects downstream, indicated by the point of lowest velocity on images D, E and F. Interestingly, for the rigid blade at image F, the angle of attack is approximately 0° yet there is clearly already a large degree of trailing edge separation, with the velocity at the trailing edge almost zero. This is thought to be due to the combination of the separation that started in image C convecting off the end of the foil, and the trailing edge vortex which begins to develop due to the increasing α. The result is that, by the time the flow returns to the beginning of a wave period, there is a large trailing edge vortex generated with counterclockwise circulation which decreases the total foil circulation. This explains the discrepancy between the loading predicted for the final stage of a wave period by the numerical model for the rigid blade and the experimental results, see figure 7.

Comparing with the flexible blade, the same separation, and convection downstream, can be seen in image C, but to a smaller degree and the images are very comparable between points C and E. The difference in flow behaviour lies in the fact that, given that the trailing edge of the flexible foil is free to deflect, it has deflected upwards in response to the high velocity at point F and the volume of low-speed flow resulting from the separation is significantly lower than for the rigid blade. As a result the experimental loading measured matches well with the attached flow analysis of the numerical model.

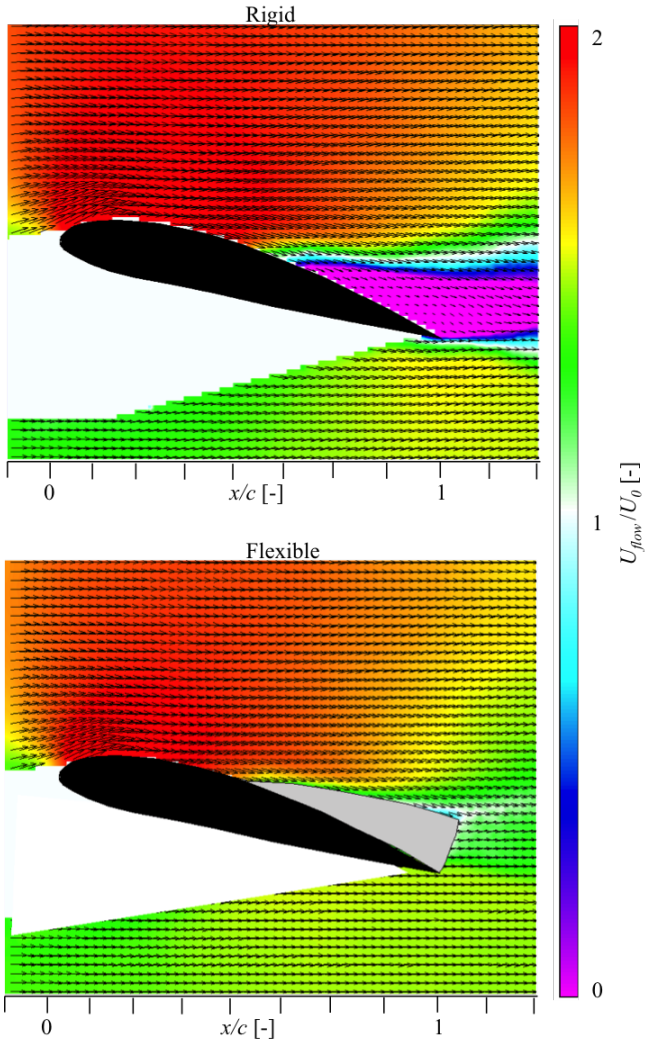

Figure 9. Time averaged velocity fields around the rigid and flexible.

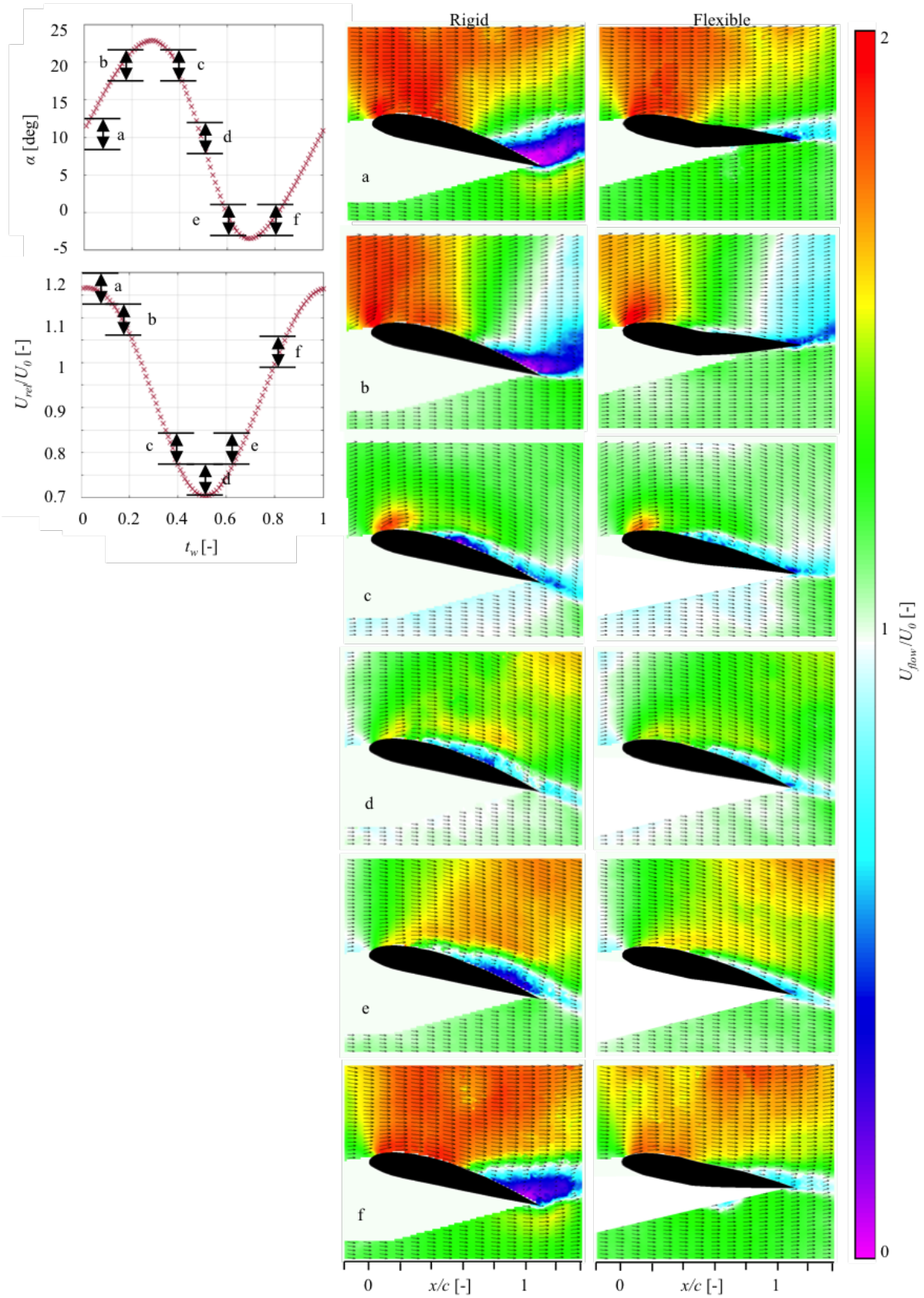

Figure 10. Velocity field around the rigid and flexible hydrofoil at 6 instants in a wave period. Inserts at the top left of the figure show the corresponding instantaneous angle of attack and flow speed (arrows show the intervals over which the flow fields have been averaged).

Further work is required in order to quantify the effect of the blade rotation, which has been ignored in this work. Furthermore the rough seabed and flood and ebb of the tide results in a constantly varying horizontal shear layer which should be accounted for when carrying out a full analysis of the unsteady loadings. In a similar vein, tower shadow and flow turbulence should also be included. The approach used in this study also relied on superimposing a wave field on a current, with the assumption being that the mean flow field is that of the current alone. Whilst this has given reasonable results here, recent work [11] suggests that surface waves actually alter the mean flow profile which should also be accounted for too.

3. CONCLUSION

A numerical model for estimating loads on both rigid and flexible blades was presented and compared with load measurements on two hydrofoils, one rigid one flexible, in combined waves and currents with opposite directions. Particle image velocimetry was used to investigate the flow field surrounding the hydrofoils, and the lift and drag on the hydrofoils were measured. The following conclusions are drawn.

- The periodic wave-induced flow fluctuations experienced by a tidal turbine blade, or a generic submerged hydrofoil, can lead to highly unsteady effects, including chord-normal forces more than 20% higher than in the current only case.
- The quasi-static chordwise pressure gradient on the upper side of the hydrofoil varies due to the wave-induced angle of attack oscillations. The background horizontal pressure field also varies because of the periodic free surface oscillations. These two pressure gradients are in phase, leading to a periodic very large combined pressure gradient which triggers boundary layer separation on the upper side of the hydrofoil at every wave period.
- A passively flexible blade is capable of reducing the amplitude of load fluctuations through decreasing the angle of attack variations, thus reducing separation and drag at high flow angles of attack. This results in a higher lift over drag ratio and so shows promise for improving the design of tidal turbine blades.

ACKNOWLEDGMENTS

The authors would like to acknowledge Dr Ton Van den Bremer for insightful discussions related to this article. This work was supported by the EPSRC, grant number EP/M02038X/1.

REFERENCES

[1] Marsh, G., 2009. "Wave and Tidal Power - an emerging new market for composites". *Reinforced Plastics*, pp. 20–24.

[2] Norris, J., and Droniou, E., 2007. "Update on emec activities, resource description, and characterisation of wave-induced velocities in a tidal flow". *Proc. 7th European wave and tidal energy Conference, Porto, Portugal*.

[3] Lachenal, X., Daynes, S., and Weaver, P. M., 2013. "Review of morphing concepts and materials for wind turbine blade applications". *Wind Energy,* **16**, pp. 283–307.

[4] Xiao, Q., and Zhu, Q., 2014. "A review on flow energy harvesters based on flapping foils". *Journal of Fluids and Structures,* **46**, pp. 174–191.

[5] Barltrop, N., Varyani, K., Grant, A., Clelland, D., and Pham, X., 2007. "Investigation into wave-current interactions in marine current turbines". *Proc. IMechE Part A: J. Power and Energy,* **221**, pp. 233–242.

[6] Galloway, P., Myers, L., and a.S. Bahaj, 2010. "Studies of a scale tidal turbine in close proximity to waves". *3rd International Conference on Ocean Energy (ICOE 2010), 6 October, Bilbao*(1), pp. 3–8.

[7] Luznik, L., Flack, K. a., Lust, E. E., and Taylor, K., 2013. "The effect of surface waves on the performance characteristics of a model tidal turbine". *Renewable Energy,* **58**, pp. 108–114.

[8] Milne, I., Day, A., Sharma, R., and Flay, R., 2013. "Blade loads on tidal turbines in planar oscillatory flow". *Ocean Engineering,* **60**, Mar., pp. 163–174.

[9] Galloway, P. W., Myers, L. E., and Bahaj, A. S., 2014. "Quantifying wave and yaw effects on a scale tidal stream turbine". *Renewable Energy,* **63**, pp. 297–307.

[10] Tarzanin, 1972. "Prediction of control loads due to blade stall". *J Am Helicopter Soc,* **17**, pp. 33–46.

[11] Olabarrieta, M., Medina, R., and Castanedo, S., 2010. "Effects of wave-current interaction on the current profile". *Coastal Engineering,* **57**(7), pp. 643–655.

[12] Dean, R. G., and Dalrymple, R. A., 2000. *Water wave mechanics for engineers and scientists*. Advanced Series on Ocean Engineering - Volume 2. World Scientific.

[13] Buvat, C., and Martin, V., 2010. Identification of test requirements and physical model design. Tech. Rep. WG4 WP1 D1, EDF.

[14] Saliveros, E., 1988. "The aerodynamic performance of the NACA-4415 aerofoil section at low Reynolds numbers". PhD thesis, University of Glasgow.

[15] Robinson, A., Ingram, D., Bryden, I., and Bruce, T., 2015. "The effect of inlet design on the flow within a combined waves and current flumes, test tank and basins". *Coastal Engineering,* **95**, pp. 117–129.

[16] Burton, T., Jenkins, N., Sharpe, D., and Bossanyi, E., 2011. *Wind Energy Handbook (Google eBook)*.